Simulations of the solar orbiter spacecraft interactions with the solar wind: effects on RPW and SWA/EAS measurements

S. Guillemant, M. Maksimovic, A. Hilgers, P. Louarn, V. Génot, C.J. Owen, J.C. Matéo Velez, P. Sarrailh, S. Hess, F. Pantellini, et al.

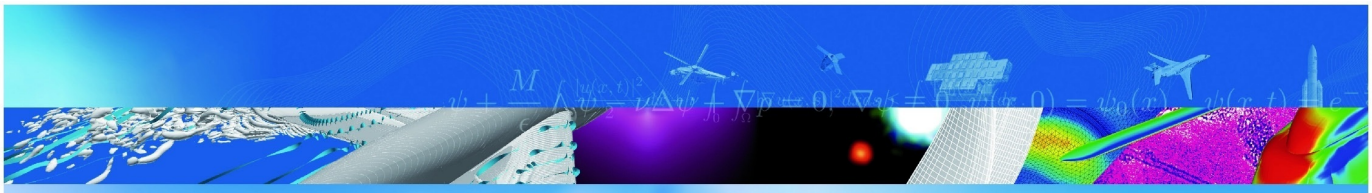

COMMUNICATION A CONGRES

Simulations of the solar orbiter spacecraft interactions with the solar wind: effects on RPW and SWA/EAS measurements

S. Guillemant, M. Maksimovic, A. Hilgers, P. Louarn, V. Génot, C.-J. Owen, J.-C. Matéo-Vélez (ONERA), P. Sarrailh (ONERA), S. Hess (ONERA), F. Pantellini, L. Lamy, A. Vecchio

SCTC 2016

NOORDWIJK, PAYS-BAS

4-8 avril 2016

TP 2016-489

70 2016 ans

ONERA

THE FRENCH AEROSPACE LAB

SIMULATIONS OF THE SOLAR ORBITER SPACECRAFT INTERACTIONS WITH THE SOLAR WIND: EFFECTS ON RPW AND SWA/EAS MEASUREMENTS

Guillemant S.[1,2], Maksimovic M.[1], Hilgers A.[3], Louarn P.[2], Génot V.[2], Owen C.J.[4], Matéo-Vélez J.-C.[5], Sarrailh P.[5], Hess S.[5], Pantellini F.[1], Lamy L.[1], Vecchio A.[1]

[1]LESIA/CNRS, Observatoire de Paris, Section de Meudon, 5 place Jules Janssen, 92195 MEUDON Cedex, France, Email : milan.maksimovic@obspm.fr
[2]IRAP, 9, avenue du Colonel Roche, BP 44346, 31028 Toulouse Cedex 4, France, Email : stanislas.guillemant@irap.omp.eu
[3]ESA/ESTEC, Noordwijk, The Netherlands, Email : alain.hilgers@esa.int
[4]MSSL/UCL, Dorking, Surrey, United Kingdom, Email: c.owen@ucl.ac.uk
[5]ONERA, 2 Avenue Edouard Belin, 31000 Toulouse, France, Email: jean-charles.mateo_velez@onera.fr

ABSTRACT

We present numerical simulations of the future Solar Orbiter spacecraft/plasma interactions performed with the Spacecraft Plasma Interaction System (SPIS) software. This spacecraft, to be launched in October 2018, is dedicated to the Sun observation with in-situ and remote sensing instruments, brought as close as 0.28 A.U. from our star. In this hot and dense environment, the entire satellite will be submitted to high radiations and temperatures (up to 10 Solar constants). Material responses to environment constraints (heat, U.V. flux, photoemission, secondary electron emission under electron impact ï SEEE ï or under proton impact - SEEP) might bias the scientific instrument measurements. Our interest is focused on two instruments: the Radio and Plasma Waves (RPW) and the Electron Analyzer System (EAS).

1. INTRODUCTION

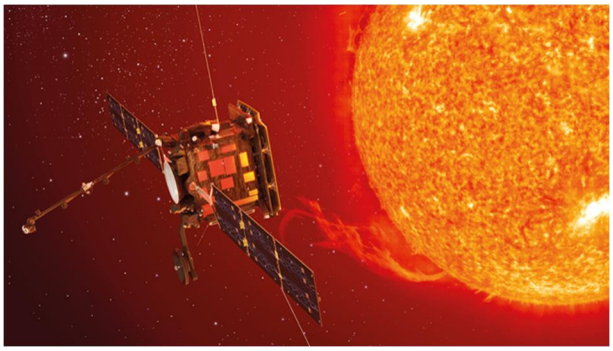

Figure 1. Solar Orbiter near the Sun (credit: ESA)

The Solar Orbiter spacecraft (SC) (see Fig. 1), to be launched in 2018, is an ESA Medium-class mission from the Cosmic Vision program 2015-2025, with NASA participation. This satellite will orbit the Sun between 1.4 and 0.28 A.U., observing our star from both in and out of ecliptic regions thanks to an inclination of 25° during nominal mission operation and potentially increased to 34° during extended mission. The mission aims at understanding the solar activity effects on the inner heliosphere functioning, by studying solar wind, magnetic field, solar transients, eruptions, corona, é This Solar Orbiter quest for answers leans on numerous embedded *in-situ* and remote sensing instruments to provide key data for comprehension of our star behaviour, and probably other ones we cannot reach at the moment.

Two instruments among the various ones embedded retain our attention for this work, their locations are indicated on Fig. 2. The first one is the Radio and Plasma Waves device (RPW) consisting in three conducting antennas of more than 6 m length which will measure at high time resolution the ambient electric and magnetic field fluctuation from DC to several kHz and determine the characteristics of electromagnetic and electrostatic waves in the solar wind. According to local environment conditions the stacers will charge independently and potential differences between them will allow to recover the ambient electric field in the plasma, knowing the effective length of the antennas.

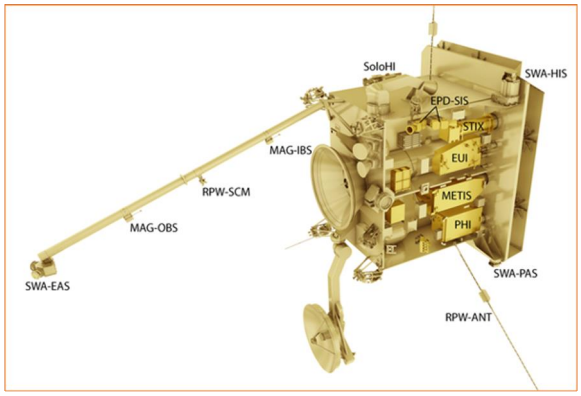

Figure 2. Localisation of Solar Orbiter scientific instruments on the spacecraft (credit: ESA)

The second instrument is the Electron Analyzer System (EAS) which is a part of the Solar Wind plasma Analyzer (SWA). EAS must measure the electron bulk properties (including density *N*, velocity *V*, and temperature *T*) of

the solar wind, between 0.28 and 1.4 AU from the Sun. It is a pair of top-hat electrostatic analyzers with aperture deflection plates mounted in the shadow of the spacecraft at the end of the instrument boom. The two sensors provide an almost full 4 ´ sr field of view subject only to minor blockage by the spacecraft and its appendages. The sensor will measure electron fluxes in the energy range from 1 eV to 5 keV, with the energy resolution 10ī 12% and an angular resolution of 10 degrees. Moments of the electron distribution will be returned with a cadence of 4 s, although the sensor will be capable of returning full 3D distributions at lower cadence, and 2D electron pitch angle distributions at 0.125 s cadence during short periods of burst mode.

As explained earlier, Solar Orbiter will approach the Sun as close as 0.28 A.U. in a hot and dense environment, submitting the entire satellite to high radiations and temperatures (up to 10 Solar constants). Material responses to environment constraints (heat, U.V. flux, photoemission, secondary electron emission) might bias the scientific instrument measurements. Previous numerical simulations [1] already showed the EAS detector will be affected by important fluxes of low energy secondary and photoelectrons, emitted by Solar Orbiter itself, and deflected by local potential barriers due to covering material charging, ion wake and secondary electron / photoelectron high densities. These phenomena result in a bias of the measured thermal electrons Energy Distribution Functions (EDF). Compared with theoretical undisturbed EDF, EAS measures a high increase of density (of more than 130% at Solar Orbiter perihelion) and a discrepancy in electron flux origin due to particle deflections generated by the satellite itself and its various element electrostatic potentials. For RPW the 3 antennas will emit electron clouds in their vicinity (modifying the local electrostatic pattern). They also might bend due to material expansion on their sunlit faces (at the closest distance to the Sun, temperature expected on the antennas is estimated to reach 500-600° C.). Finally, Solar Orbiter body elements covered with dielectric materials might charge to disturbing potentials for natural electric fields estimations.

This is the reason why numerical simulations are necessary, in order to estimate the disturbances and the artificial part of biases on measurements (the fraction due to the spacecraft itself). The Spacecraft Plasma Interaction System (SPIS) [2] software is used to provide simulations of Solar Orbiter charging and its RPW and EAS instrument measurements. The SPIS project aims at developing a software toolkit for spacecraft-plasma interactions and spacecraft charging modelling. Its numerical kernel is a 3D unstructured Particle-In-Cell plasma model (PIC). Recent improvements allow the code to simulate within the simulation box scientific instruments (Langmuir probes, particle detectors, é) and their associated measurements.

In the following, SPIS simulations of Solar Orbiter at its perihelion will be presented, considering or not a surrounding electric field and its effect on RPW potentials and effective lengths. In a second part, spacecraft/plasma interaction impacts on EAS measurements will be analyzed, especially energy distribution functions (including parasite electrons such as secondary and photoelectrons), biases on the moments due to spacecraft charging and particle emission, incoming particle flux direction and deviation due to electrostatic sheath.

This preliminary work aims at comprehending future real inflight measurements, hopefully with good estimations of the data corrections necessary to get back to the undisturbed local plasma environment.

2. SIMULATION CONFIGURATION

2.1. Geometry model

Our spacecraft configuration used for those simulations is presented on Fig. 3. It is a simplified model of the satellite (made with the *Gmsh* software, the SPIS embedded CAD modelling tool) as we evidently cannot reproduce in full details the real structure. The main elements have been modelled in 3D, respecting their real (or sometimes supposed) dimensions as known and communicated when the work was performed. Some lengths might still change depending on industrial constraints, as for the covering materials. Concerning the latest: some assumptions had to be made to define them for SPIS. Indeed, some were unknown by our team or still under definition by contractors when this work has been performed. It can be specified that in the following case all surfaces are conducting except for the two front faces of the solar arrays.

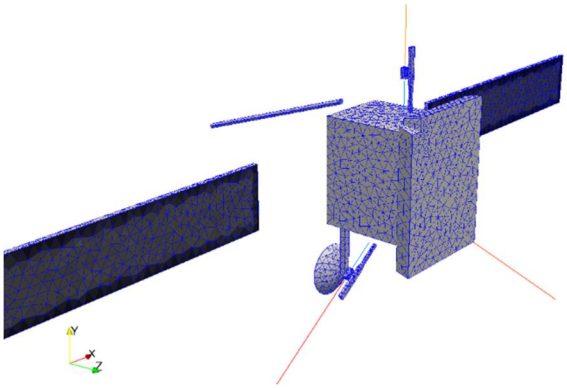

Figure 3. Gmsh model of Solar Orbiter used in SPIS

On Fig. 3 we can notice the main structure elements: satellite body, sunshield, High Gain Antenna (HGA) dish and its mast, two solar arrays and rear boom at the rear, which end will carry the EAS instrument (not yet represented on this model). RPW elements also appear: three thin antennas of 6.5 m long (and an average radius of 1.3 cm) in red, three booms (also modelled as thin

wires) in blue and a set of three sunshields aiming at shadowing the preamps boxes (in which the stacers will be stowed during launch). Once meshed (this step is done automatically with Gmsh through an unstructured 3D mesh of tetrahedra which characteristic dimensions are user defined), the model in its volume (an ovoid of about 36 × 36 × 40 m) represents ~340000 cells.

2.2. Environment and SPIS parameters

Environment parameters	Values at 0.28 AU from the Sun
Sun flux (# 1 AU)	12.76
N of Electron and $H+$(m^{-3})	1.04×10^{8}
Electron temperature (eV)	21.37
Proton temperature (eV)	27
Spacecraft velocity in X direction (m/s)	60000.0
Spacecraft velocity in Z direction (m/s)	400000.0
Magnetic field in -Z direction (T)	4×10^{-6}
Debye length (m)	3.4

Table 1. Environment parameters used in SPIS simulations

We place the study at Solar Orbiter perihelion, *i.e.* at 0.28 A.U. from the Sun. Following plasma parameters as used in SPIS are displayed in Tab. 1. All species (protons, thermal electrons, secondary electrons and photoelectrons) are computed using a PIC model. The secondary electron emission under electron impact (SEY), as the secondary electron emission under proton impact (SEP), are set with a characteristic energy of 2 eV (Maxwellian velocity distribution function). The backscattered electrons are emitted with 2/3 of their initial energy and photoelectrons are emitted with a Maxwellian energy proýle with temperature of 3 eV. The Sun is located in the -*Z* direction, normal to the sunshield. In order to apply an electric field over the simulation box (constant over time and unidirectional) with SPIS we have to use the $\boldsymbol{V} \times \boldsymbol{B}$ induced $\boldsymbol{E}$ field (where $\boldsymbol{V}$ is the spacecraft velocity according to its motion along its orbit and $\boldsymbol{B}$ a constant magnetic field). In this case we consider a strong unrealistic magnetic field in order to clearly see field effects on the RPW antennas. In a further work a more realistic environment will be applied. According to the configuration indicated in Table 1, the induced electric field is here set to E_Y = 240 mV/m. Note that almost all conducting surfaces are directly connected to the spacecraft ground, meaning that those will have their potential floating at the same value that the Solar Orbiter body. The external surfaces of dielectric elements will charge differentially. However, we apply a capacity between the three RPW antennas and the satellite ground in order to decouple those wires from the body and be able to obtain different potentials on them.

3. SIMULATION OF RPW ANTENNAS

3.1. Simulation results

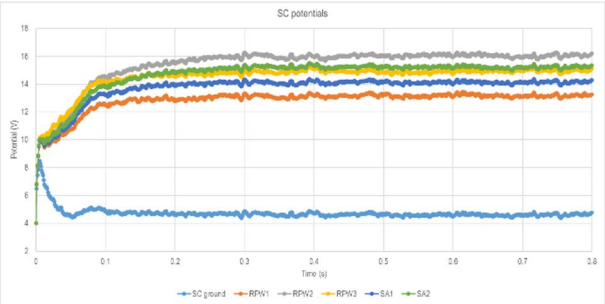

Figure 4. Spacecraft potentials versus time

In this first case, as illustrated in Fig. 4, spacecraft potentials settle to steady values after a transitory regime of here 0.4 s, due to the instantaneous Sun lightning of the satellite inherent to simulation start. Steady potentials reached by satellite elements are displayed on Tab. 2. These are average values calculated between t = 0.4 and t = 0.8 s. Standard deviations of those values during this period are also indicated as a proof of numerical stability. The two solar panels sunlit faces are identified as SA1 (on the -*X* side of the simulation box) and SA2 on the opposite side. The three antennas are identified as RPW1 along the *Y* axis, RPW2 towards -*X* and RPW3 on the +*X* side of the simulation box.

In average after t = 0.4 s	Potential (V)	Standard deviation (V)
SC ground	4.61	0.08
RPW1 (+*Y*)	13.17	0.09
RPW2 (-*X*)	16.04	0.11
RPW3 (+*X*)	14.93	0.10
SA 1 (-*X*)	14.13	0.09
SA 2 (+*X*)	15.23	0.08

Table 2. Average steady potentials on Solar Orbiter elements

Concerning plasma potential in the volume, Fig. 5 shows the electrostatic sheath in the *X*-*Z* plane (*Y*=0) passing by the centre of the sunshield and solar panels. Negative potential areas appear in front of the spacecraft (because of high densities of secondary and photoelectrons) and behind it because of an ion wake (proton bulk is flowing along -*Z*) and high densities of secondary electrons. Maximum potential of 15.2 V is on the front face of the -*X* sided solar array. Behind the satellite body the tip of the rear boom reaches the *Y=0* plane, explaining the positive potential in this area. Fig. 6 displays the sheath in the RPW plane containing the three antennas. This cut also shows the influence of the solar array cover glasses in the vicinity of the stacers. Those two last illustrations are considered in the reference frame of the plasma. Fig. 7 is the ion density map in the *X*-*Z* plane, clearly showing the ion depletion due to the combination of the proton bulk velocity towards -*Z* and the Solar Orbiter velocity

towards the +*X* direction. This phenomenon has already been explained in [3].

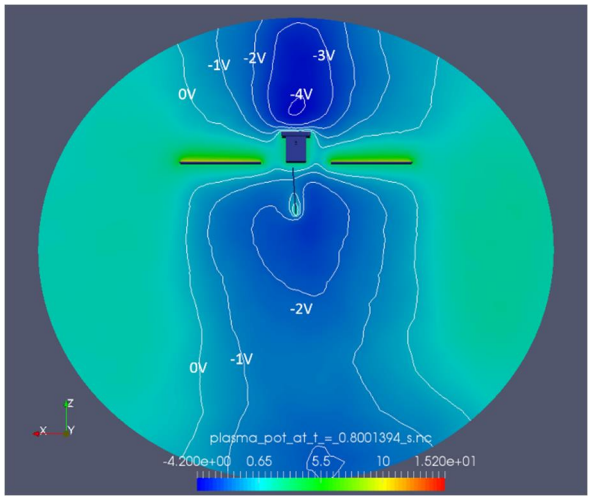

Figure 5. Plasma potential (V) in the X-Z plane

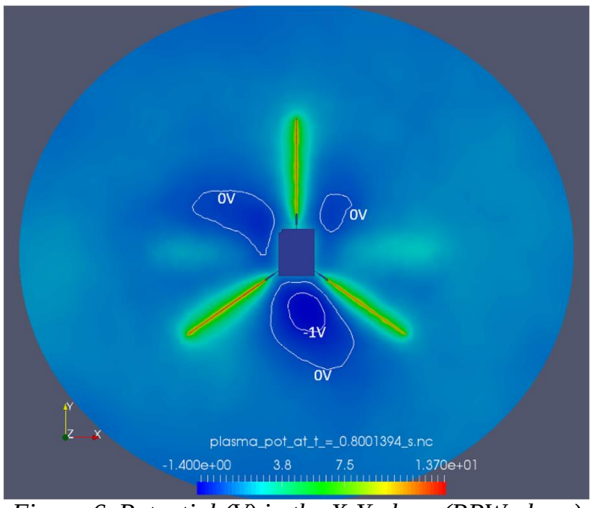

Figure 6. Potential (V) in the X-Y plane (RPW plane)

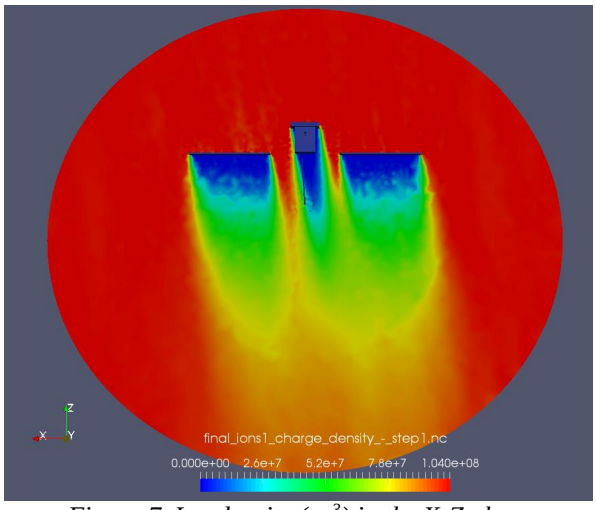

Figure 7. Ion density (m^{-3}) in the X-Z plane

Interest of this simulation is to recover the effective length *Leff* of the RPW antennas. Indeed, the measured electric field $\boldsymbol{E}_{AB}$ between, for instance, antennas *A* and *B* can be expressed as $\ddot{\boldsymbol{u}}_{AB} = \boldsymbol{Leff}_{AB} \cdot \boldsymbol{E}_{AB}$. In numerical simulations, knowing the user defined $\boldsymbol{E}_{AB}$ and $\ddot{\boldsymbol{u}}_{AB}$ obtained we can deduce $Leff_{AB}$. This reasoning is sketched on the left. In our case we display the various $\ddot{\boldsymbol{u}}$ obtained in Tab. 3.

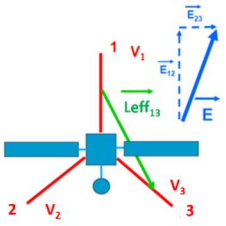

In average after t = 0.4 s	Potential (V)	Standard deviation (V)
qū 1-2 = ū 1 ï ū 2	-2.87	0.07
qū 1-3 = ū 1 ï ū 3	-1.76	0.08
qū 2-3 = ū 2 ï ū 3	1.11	0.11

Table 3. Average differences of potential on RPW antennas

Considering our CAD model, real effective lengths dimensions and directions between RPW stacers (*i.e.* distances between farthest, medium and closest points of antennas from the satellite body) are displayed on Fig. 8. It also appears on this Figure that here: $\boldsymbol{E}$ is along *Y* axis and corresponds to E_Y= 240 mV/m. We thus need to consider the $\boldsymbol{E}_{//}$ component of this field which is actually applied on RPW 1-2 and 1-3 combinations, as in this case $Leff_{23}$ corresponds to the null perpendicular $\boldsymbol{E}$ component. $\boldsymbol{E}_{//}$ has the same value for $Leff_{12}$ and $Leff_{13}$: $\boldsymbol{E}_{//} = \boldsymbol{E} \times \cos \boldsymbol{b}$ = 0.21 V/m (with $\boldsymbol{b}$ = 27.5° the angle between $Leff_{12}$ and $\boldsymbol{E}$). Corresponding lengths are then: $Leff_{12}$ = 13.66 m and $Leff_{13}$ = 8.38 m. Looking at Fig. 8 it can be noticed that the average effective length obtained (11 m) is between medium and maximum real lengths.

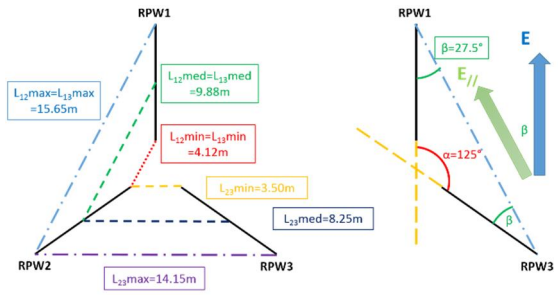

Figure 8. RPW configuration and effective lengths

In a first consideration, one would suppose that with $\boldsymbol{E}$ along *Y* axis, a symmetric spacecraft geometry and the same illumination of antennas we should get $Leff_{12} = Leff_{13}$, while we actually obtain more than 5 meters of discrepancy. This is due to the combination of $\boldsymbol{E}$, $\boldsymbol{B}$ and $\boldsymbol{V}_{SC}$ which will submit all charged particles to different forces, affecting their motion in the volume. Indeed, considering following equation:

$$\boldsymbol{F} = \frac{d\boldsymbol{p}}{dt}, \quad (1)$$

the drift velocity will push electrons towards -*X* direction, while their gyration:

$$\frac{}{}, (2)$$

will confine them around the magnetic field lines. For secondary and photoelectrons $v_d \sim -6 \times 10^4$ m/s in the *X* direction (opposite to V_{SC} but of the same order) and $r \sim 1$ m. Those phenomena engender specific particle volume distribution as illustrated on Fig. 9 (for photoelectrons).

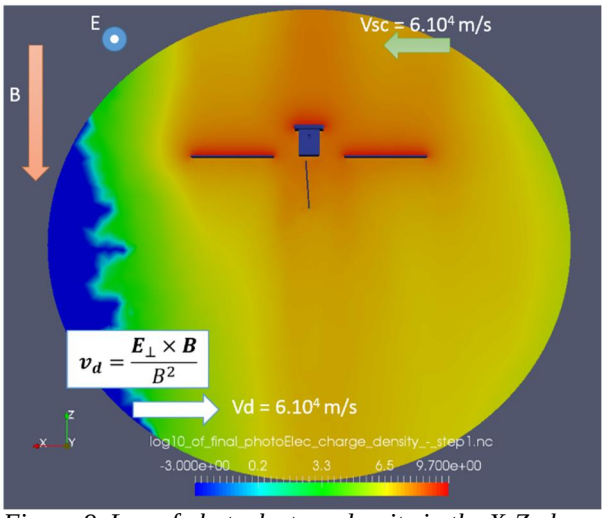

Figure 9. Log of photoelectron density in the X-Z plane

On this Figure the combination of $\boldsymbol{v_d}$, $\boldsymbol{V_{SC}}$ and $\boldsymbol{B}$ clearly spread out along $\boldsymbol{B}$ and shift towards -*X* direction the photoelectron cloud. Secondary electrons under electron and proton impacts behave similarly. So looking this population density in a plane containing RPW antennas (Fig. 10) demonstrates how RPW2 and 3 do not charge at the same potential, as particle fluxes of low energy electrons between them are different and not symmetric.

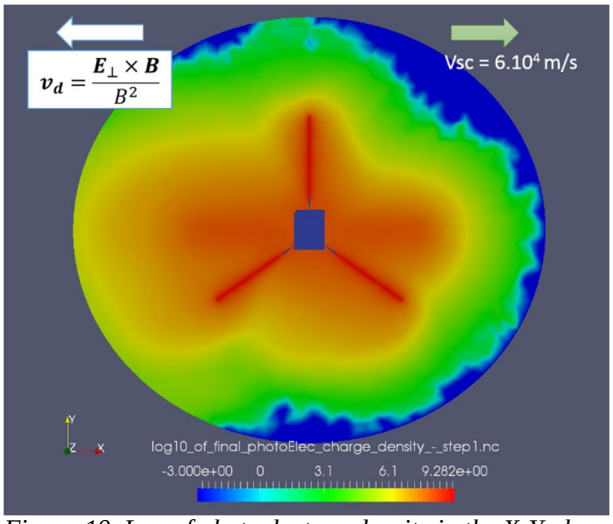

Figure 10. Log of photoelectron density in the X-Y plane

3.2. Conclusion for RPW antennas

With this first analysis we demonstrated how SPIS simulations can help predict and understand RPW behaviour in a perihelion situation. Even though the here-presented case does not reflect a realistic one (especially concerning the magnetic field orientation and intensity), it already helps preparing new simulation cases to get deeper into RPW antenna reaction understanding. Specific case with particle drift velocity direction normal to the RPW plane, and so cancelling potential discrepancy between RPW2 and 3, has already been performed and will be presented in the next future. New data concerning Solar Orbiter materials and updates are also being applied to our model to match the future satellite and instrument design.

4. SIMULATION OF EAS INSTRUMENT

In the following a simulation of the Electron Analyzer System measurement at perihelion will be presented. This case was performed a certain time ago [1], without considering any electromagnetic field. The spacecraft geometry used at this time is now outdated but globally respects main element dimensions and configurations. In the near future EAS numerical model will be implemented into the case presented in Section 3. But the following already presents new SPIS capabilities of modelling numerical particle detectors and what type of outputs we want to obtain.

4.1. Numerical EAS modelling and simulation configuration

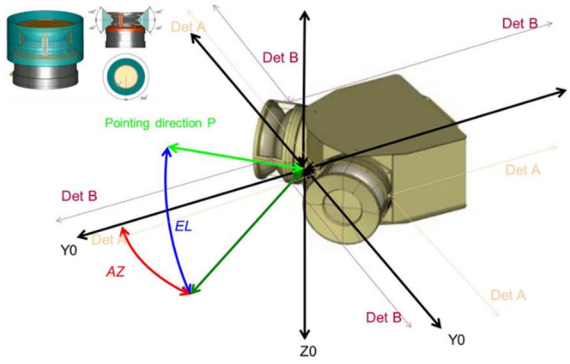

Figure 11. EAS CAD model and configuration

EAS technical properties have already been introduced in Section 1. Its design is displayed on Fig. 11 and GMSH model of the instrument used in SPIS on Fig. 12.
For this type of detector, with particle entrance for each EAS sensor as a circular ring, it is necessary to consider each EAS entrance as the sum of eight curved surfaces, in order to limit the curvature of each surface detector. Indeed, each surface is considered in SPIS model as a particle detector with a unique local detector basis (X_D,

Y_D, Z_D) deýned so as the Z_D axis is pointing into the detector, normal to the surface. This deýnition allows deýning properly the acceptance angles for incoming particles in this basis. This is why each particle detector has to remain relatively "þat". The EAS instrument is thus composed in this model of 16 particle detector surfaces, each one providing its own outputs which will have to be combined for a global overview of EAS results. For all cases presented here the acceptance angles are ±90° in azimuth (*AZ*) and ±45° in elevation (*EL*). This way the entire ýeld of view of both detectors covers the 4´ sr of the environment, as in reality.

Plasma parameters are identical to the ones presented on Table 1. *Environment parameters used in SPIS simulations*except that we do not consider any magnetic field or a spacecraft velocity in *X* direction. Simulation configuration is the same that was detailed in Section 2.2. EAS outputs are presented hereafter.

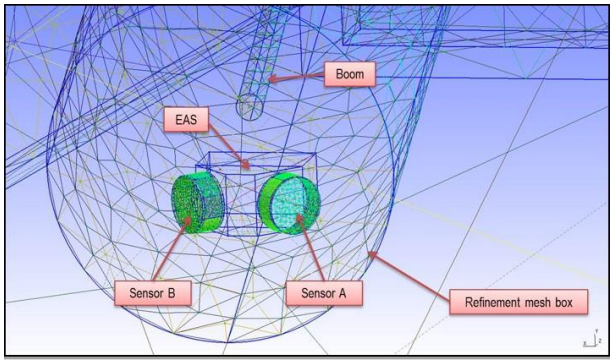

Figure 12. GMSH model for EAS used in SPIS

4.2. EAS results

For this case without ***B***, this spacecraft geometry and covering materials, all conducting Solar Orbiter surfaces (including EAS) are set at +3.1 V. Front faces of solar arrays (dielectric) are charged at +14.1 V, and the High Gain Antenna (HGA, dielectric at this time), is charged at a potential of +9 V.

We can quickly take a look to the global plasma behaviour around our object. For instance, potential in the *X-Z* plane (Fig. 13), shows that we recover same electrostatic phenomena in the ram (high densities of secondary and photoelectrons, as it appears on Fig. 14) and the in wake (lack of protons and high density of secondary particles). Contrary to previous RPW case including ***V***×***B*** effect: no drift or expansion of low energy electrons appears for this situation.

Then, what does EAS measure? First letôs have a look on the Energy Distribution Function (EDF) of thermal electrons. The environment yellow curve is the electron distribution from environment as described in Table 1. *Environment parameters used in SPIS simulations*, and the one that EAS should measure if there were no plasma disturbances due to spacecraft/plasma interactions.

The orange curve *FE(E)*, represents the environment that should be theoretically measured by EAS if there was only this instrument charged at its potential of +3.1V in the simulation box, with no spacecraft, no wake or any potential barrier around EAS. It is calculated analytically using Liouvilleôs theorem [3]. This distribution function is thus based on the true environment, but shifted of 3.1 eV (indeed no electrons can reach the detector with a potential energy inferior to EAS potential), and increased after 3.1 eV because of the attracting electric potential of EAS.

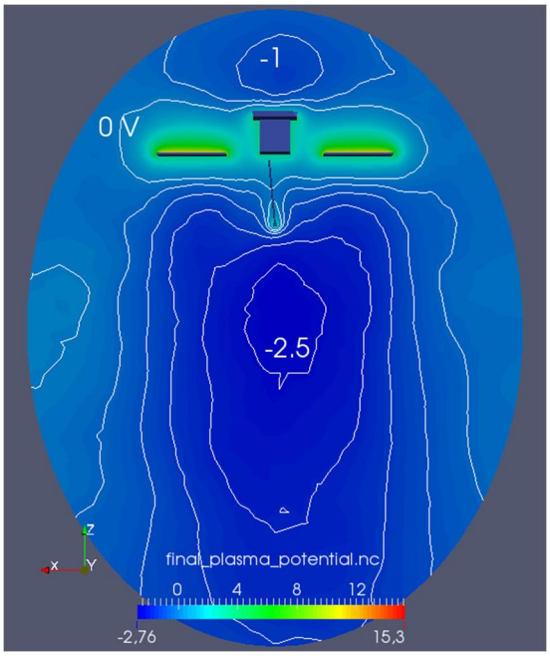

Figure 13. Plasma potential around Solar Orbiter in the X-Z plane

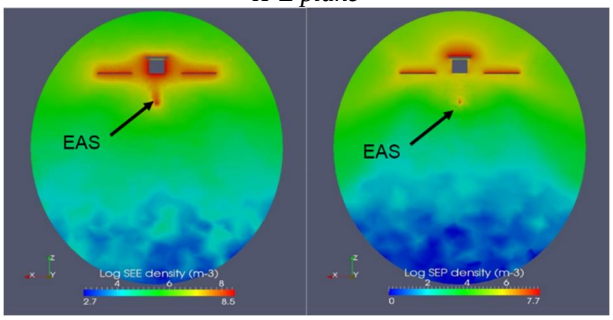

Figure 14. Log of secondary electron (left) and photoelectron (right) density in the X-Z plan

Finally, the blue curve *Energy DF FG* represents the simulated measurement of thermal electrons. The measurement results in a combination between the true environment and the theoretical measure of EAS alone. Indeed, the analytical modelling using Liouvilleôs theorem assuming all possible trajectories are ýlled regarding the expected distribution function in a local non zero potential is only valid for a single detector immersed in the plasma. As here the entire Solar Orbiter

structure is positively charged (at values that can reach +14.1 V on the Solar panels), many thermal electrons are attracted in those areas and fewer on EAS detectors which results in a lack of information on the low energy electrons in the simulated measures. It can be seen on the difference of amplitude between the maximums of the blue and orange curves.

The corresponding densities calculated through integration of thermal electrons *EDF* (Fig. 13) are:

- Undisturbed environment (yellow): $N_0 = 1.04\times10^8$ m^{-3}. Same values are found as this model is practically not truncated (the highest temperature considered is 200eV *i.e.* almost 10 times the thermal electrons temperature modelled),
- Theory (orange): $N_{theo} = 1.16\times10^8$ m^{-3} > N_0 because of EAS potential (+3.1 V),
- Measurements (blue): $N_{meas} = 1.01\times10^8$ m^{-3} < N_{theo} because of the spacecraft charged structure and the plasma disturbances (ion wake, solar panels, HGA, potential barriers).

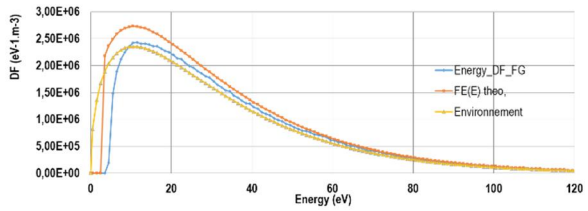

Figure 15. Energy distribution functions of thermal electrons on EAS

It can be noticed that the simulated electron measurements (blue curve) is lower than the theoretical red curve (analytical model): it sounds like low energy electrons (visibly between 3 and 5 eV) are missing. The explanation is that the EAS instrument is surrounded by negative potential barriers between -1.5 and -2.5 V: they ýlter the low energy electrons. The particles which cross those barriers are then accelerated by EAS potential. The minimum energy of those elements becomes: 1.5 + 3.1 = 4.6 eV. Negative potentials around the particle detector increase the SEEE densities through electron impacts. *EDF* reaches 5×10^7 m^{-3}.eV^{-1} for SEEE and 2.5×10^6 m^{-3}.eV^{-1} for the primary electrons (factor 20).

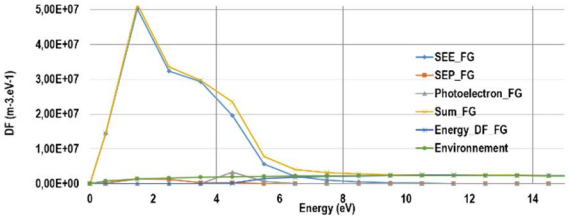

Figure 16. Energy distribution functions of all electrons on EAS

The simulated measurements of thermal electrons give a discrepancy of 2.8% regarding N_0. Adding to the measurements photoelectrons, SEEE and SEEP (Fig. 16) gives a total density of measured electrons (the purple *Sum* curve) of $N_{total} = 2.42\times10^8$ m^{-3} (a difference of 132% regarding N_0). The low energy ranges are highly dominated by SEEE.

Other results produced with post processing the particle detector outputs are the 2D maps of detection of thermal electrons regarding EAS pointing direction (Fig. 17). They can provide information regarding the instrument ýeld of view and help answer questions such as: where are the physical or electrostatic obstacles to electron detection and what are the consecutive impacts on measurements, from which directions come the highest/lowest particle þuxes, *etc*. The EAS detailed ýeld of view, with deýnition of pointing angles azimuth (AZ) and elevation (EL), was presented on Fig. 11. The limits of AZ acceptance when EL = 0° are also represented (with thin purple and orange arrows) to show that both sensors are needed to cover the entire ýeld of view. Fig. 17 is the counting map of thermal electrons detected by the entire EAS instrument, regarding the pointing direction (AZ and EL angles). In order to compute this map, it was necessary to create bins in AZ and EL (10° bins in this case) constituting the angular resolution (and similar to the real EAS angular resolution). Only electrons with less than 15 eV energy have been treated (as low energy electrons are the most disturbed by the spacecraft presence in the environment).

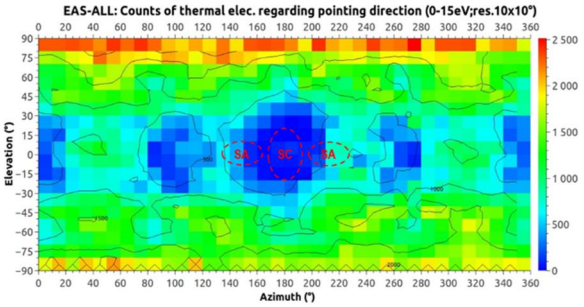

Figure 17. Counting map of thermal electrons detected by EAS

Note that other types of resolution/energy ranges can be of course selected to better ýt other requirements. In red are indicated the objects pointed with the corresponding values of AZ and EL: the Solar Arrays (SA) and the spacecraft body (SC) when looking behind EAS (note that the objects positions are quite approximated). The bin colors (from blue to red) indicate the number of electrons counted in each bin direction. In the same Fig. 17 the effect of the physical body clearly blocking particle arrival is manifest. The Solar panels do not visibly affect detection in their speciýc direction as they are quite thin regarding the bin precision and close to the spacecraft body. At AZ ~ 90° and ~ 270° (and EL~ 0°)

there is a lower particle detection due to several causes. First the pointing direction skimming or targeting the charged detectors themselves. Indeed, it appears in Fig. 11 that at AZ ~ 90° and a null elevation, detector B on the left points towards the detector A on the right, charged at +3 V. Secondly the connection between the two detectors ýelds of view: indeed, at these speciýc directions one detector begin its acceptance domain while the other ends it, see Fig. 11, which also explains the loss of particles when both detectors point the null AZ and EL direction. When EL ~ 0° the sensors have no common pointing directions. On the contrary the enhancement of electron detection at high EL values is simply due to a geometric factor: when EL approaches ±90°, both sensors have common pointing direction, whatever the AZ value considered. It results in an increase in particle counting. The HGA and the two lower RPW antennas have also a blocking effect on electrons (EL ~ī 45°, AZ~ 180°), this is why EAS collects fewer particles when pointing towards EL ~ -90°, rather than EL~ +90°.

4.3. Conclusion for numerical EAS measurements

This Section also showed (as for RPW antennas in previous Section) how new SPIS capabilities allow to handle numerical instrument measurements and understand those results: here concerning origin of parasite particle detection, computation of biases, *etc*. Even though this case has been performed using an outdating model of Solar Orbiter, neglecting electromagnetic fields that will definitely exist at satellite perihelion, it gives an explicit example of what our work will focus on in the next future.

5. CONCLUSION

This work represents a preliminary study of Solar Orbiter and its scientific instruments, RPW and SWA-EAS, behaviour at perihelion (0.28 AU from the Sun). Simulations show various effects that should clearly be considered in order to understand properly their measurements: surface charging and electrostatic sheath, secondary and photoelectron emission and collection, $\boldsymbol{V}\times\boldsymbol{B}$ induced electric field and corresponding drift velocity (and gyration) of low energy particles, *etc*. Combined effects of these phenomena will definitely affect and complicate surrounding environment analysis. As demonstrated in this study, numerical simulations help separate various interactions and distinguish their effects on obtained data.

Soon, those investigations will be reinforced using an updated CAD model of Solar Orbiter, RPW and EAS, plus a more accurate environment which will take into account the magnetic field and its proper orientation at the satellite perihelion. Independent currents will also be injected into RPW stacers in order to lower down their electrostatic potentials and get closer to plasma potential.

6. REFERENCES

1. Guillemant, S. Study and Simulations of Spacecraft/Plasma Interaction Phenomena and their Effects on Low Energy Plasma Measurements. *Earth and Planetary Astrophysics [astro-ph.EP]. Université Paul Sabatier - Toulouse III, 2014.*
2. Roussel, J.-F., Rogier, F., Dufour, G., Matéo-Vélez, J.-C., Forest, J., Hilgers, A., Rodgers, D., Girard, L. and Payan, D. SPIS Open Source Code: Methods, Capabilities, Achievements and Prospects. *IEEE Trans. Plasma Sci., 36, 2360ï2368, doi:10.1109/TPS.2008.2002327, 2008.*
3. Guillemant, S., Génot, V., Matéo-Vélez, J.-C., Sarrailh, P., Hilgers, A. and Louarn, P. Simulation Study of Spacecraft Electrostatic Sheath Changes With the Heliocentric Distances from 0.044 to 1 AU. *Plasma Science, IEEE Transactions on, Volume: PP, Issue: 99, 2013.*

Office National d'Études et de Recherches Aérospatiales
2 avenue Edouard Belin - BP 74025
31055 TOULOUSE Cedex 4
Tél. : +33 5 62 25 25 25
http://www.onera.fr